

High-spatial resolution measurements with a GaAs:Cr sensor using the charge integrating MÖNCH detector with a pixel pitch of 25 μm

S. Chiriotti,^a R. Barten,^a A. Bergamaschi,^a M. Brückner,^a M. Carulla,^a I. Chsherbakov,^b R. Dinapoli,^a E. Fröjd,^a D. Greiffenberg,^{a,*} S. Hasanaj,^a V. Hinger,^a T. King,^a P. Kozłowski,^a C. Lopez-Cuenca,^a A. Lozinskaya,^b F. Marone,^a D. Mezza,^a K. Moustakas,^a A. Mozzanica,^a C. Ruder,^a B. Schmitt,^a D. Thattil,^a O. Tolbanov,^b A. Tyazhev,^b A. Zarubin^b and J. Zhang^a

^aPaul Scherrer Institut (PSI),

Forschungsstrasse 111, 5232 Villigen PSI, Switzerland

^bR&D Center “Advanced Electronic Technologies”, Tomsk State University (TSU),

Lenin Ave 36, RUS-634050 Tomsk, Russia

E-mail: dominic.greiffenberg@psi.ch

ABSTRACT: The aim of this project is to determine the imaging capabilities of a 25 μm pixel pitch GaAs:Cr sensor of 500 μm thickness bump-bonded to the charge integrating MÖNCH 03 readout chip (also called GaAs-MÖNCH assembly) and to assess the possibility to improve the spatial resolution by applying a position interpolation algorithm developed at PSI.

Measurements were performed at the TOMCAT beamline of the Swiss Light Source (SLS) using photon beams in the energy range of 10–30 keV. The imaging experiments indicate the possibility to enhance the spatial resolution of the detector beyond its actual physical pixel pitch. We have quantified the spatial resolution of a GaAs-MÖNCH assembly by means of the modulation transfer function (MTF), achieving 10 μm at 10 keV and 12 μm at 20 keV photon energies. By applying a modified interpolation algorithm, a spatial resolution of $\sim 5 \mu\text{m}$ was obtained for 16 keV when binning to 2.5 μm virtual pixels, while with the silicon-MÖNCH assembly, we achieved a spatial resolution of 3.5 μm , which serves as gold standard.

The results are promising because they open new possibilities to perform imaging measurements using the GaAs-MÖNCH assembly at photon energies above 15 keV, where silicon sensors suffer from a diminishing quantum efficiency.

KEYWORDS: Hybrid detectors; Image processing; X-ray detectors

*Corresponding author.

Contents

1	Introduction	1
2	Material and methods	2
2.1	The MÖNCH detector	2
2.2	Experimental setup	3
3	Preliminary results	4
3.1	Characterization of the GaAs sensor	4
3.2	Gain calibration and noise measurement	5
3.3	Position interpolation algorithm	9
3.4	High resolution imaging with GaAs	10
3.5	Measurement of the modulation transfer function (MTF)	13
4	Conclusion and outlook	14

1 Introduction

In contrast to silicon-based sensors, high-Z sensor materials such as gallium arsenide (GaAs) provide a higher quantum efficiency for the detection of hard X-rays with energies above 15 keV, which motivates the development of GaAs X-ray detectors for imaging applications [1]. For instance, a 500 μm thick GaAs sensor (as used in this study) provides an absorption efficiency > 99% for 15 keV photons in comparison to 79%, achieved with a 650 μm thick silicon (Si) sensor [2]. The difference in absorption efficiency further increases at higher energies e.g, when using 30 keV photons, the absorption efficiency of GaAs is 97% compared to 20% when using Si.

However, high-Z sensors require a careful characterization to better understand their performance. In comparison to Si, high-Z sensors typically suffer from crystal inhomogeneities, incomplete charge collection, charge (de-)trapping effects, and high-energy fluorescence photons [3–5]. For instance, fluorescence photons in GaAs sensors are emitted at $E_{\text{Ga K}\alpha 1} = 9.25$ keV and $E_{\text{As K}\alpha 1} = 10.54$ keV, which have attenuation lengths of $\lambda_{\text{Ga}} = 40.6$ μm and $\lambda_{\text{As}} = 15.6$ μm compared to fluorescence of Si at $E_{\text{Si K}\alpha 1} = 1.74$ keV which has an attenuation length of $\lambda_{\text{Si}} = 11.9$ μm . This means that when using pixels with a dimension of 25 μm , there is a non-negligible probability in GaAs, that fluorescence photons escape from the pixel where the primary X-ray has been absorbed and deposit their energy in a neighboring pixel, degrading the spatial resolution [6, 7].

On the other hand, recent studies performed with chromium-compensated gallium arsenide (GaAs:Cr) sensors have shown that its performance is superior to previous generations of GaAs X-ray sensors without chromium compensation [8–10], encouraging the use of these sensors. In particular, GaAs:Cr bump-bonded to the charge integrating (CI) detector JUNGFRAU with 75 μm

pixel pitch has proven to be a promising X-ray detector for applications at synchrotron facilities up to photon energies of 60 keV [11].

Several studies have thoroughly characterized GaAs:Cr sensors with pixel pitches between 55 and 250 μm and encountered additional challenges such as non-uniformities leading to variations in the effective pixel size [3, 9–13].

While the charge sharing between adjacent pixels limits the minimal pixel size in single photon counting (SPC) high granularity detectors, we can take advantage of the charge shared among neighbouring pixels in CI detectors to efficiently reconstruct the photon hit position, as previously shown for Si sensors [14–16].

The novelty of this work lies in the use of a very small pixel pitch charge integrating detector, which allows to measure the charge cloud distribution of every photon with higher spatial resolution in comparison to previous works performed with high-Z sensors bump-bonded to SPC detectors [12, 17, 18].

The spatial resolution and the imaging capabilities of the 25 μm pitch MÖNCH charge integrating readout chip bump-bonded to a GaAs:Cr sensor (GaAs-MÖNCH) are compared to a MÖNCH chip combined with a 650 μm thick silicon sensor (Si-MÖNCH), which serves as a gold standard. Previous imaging measurements acquired with a Si sensor mounted to the charge integrating MÖNCH readout chip have proven that it is possible to use interpolation algorithms to enhance the spatial resolution beyond the actual pixel size, achieving a spatial resolution of the order of a few microns [14–16, 19].

First imaging experiments performed with MÖNCH combined to GaAs and Si sensors acquired at the TOMCAT beamline of the Swiss Light Source (SLS) at energies between 10 keV and 30 keV will be presented. In particular, processed images both with the physical pixel pitch and with virtual pixel pitches smaller than the native size, after applying the interpolation algorithm, will be shown in section 3.4. Moreover, a quantitative evaluation of the spatial resolution by means of determining the modulation transfer function (MTF) as a function of the energy and interpolated bin size will be presented in section 3.5.

2 Material and methods

2.1 The MÖNCH detector

The MÖNCH readout chip [20] is a charge-integrating hybrid pixel detector being developed at PSI, which has a matrix of 400×400 square pixels of 25 μm pitch covering an active area of $1 \times 1 \text{ cm}^2$. The MÖNCH 03 pixel architecture comprises a charge integrating preamplifier followed by a correlated double sampling (CDS) stage to remove low frequency noise contributions [21]. Each amplification stage offers the possibility to statically adjust the gain, thus being able to achieve the best compromise between signal-to-noise ratio (SNR) and dynamic range. Using the high gain settings in the CDS and in the preamplifier, a very low noise of 150 eV r.m.s was measured with a Si-MÖNCH assembly [16]. With the present readout system, the detector can be operated at a maximum frame rate of 1.66 kHz [15, 22].

Measurements were performed with chromium compensated GaAs (GaAs:Cr) and silicon sensors bump-bonded to the MÖNCH 03 ASIC (Application Specific Integrated Circuit) using a standard indium bump-bonding technique developed in-house at PSI [10]. GaAs:Cr sensors

Table 1. Properties and settings of the sensors used in this study. The housing of the detector was cooled with a liquid coolant (mixture of water and glycol) to a temperature of +15 °C using a chiller. See more details in [20].

Material	Thickness	Bias V	Exposure time	Gain settings
GaAs:Cr	500 μm	−300 V	6 μs	CDS gain 1 and preamp in HG (G1HG)
Si	650 μm	300 V	1 ms	CDS gain 4 and preamp in HG (G4HG)

based on LEC (Liquid Encapsulated Czochalski) material were provided by the Tomsk State University [11, 23].

In the current MÖNCH prototype, the whole signal chain was optimized for hole collection to work with p-in-n Si sensors (see further details in [20]). For a Si sensor applying high gain (HG) in the preamplifier and a gain of 4 (G4) in the CDS maximizes the total gain and minimizes the noise, still providing enough dynamic range for our tests (about 40 keV).

Conversely, in the case of GaAs:Cr sensors preferably electrons are collected. As GaAs:Cr sensors are operated as photo resistors compared to silicon sensors which are operated as diodes, the dark current of GaAs:Cr sensors is much higher than that of the silicon sensors, which leads to an increased noise and which decreases the dynamic range proportionally to the acquisition time. In order to have a comparable dynamic range of 40 keV we can keep the preamplifier in HG, but we need to use a lower gain in the CDS (G1). As a consequence, the electronic noise will be higher but still allowing single photon resolution in the energy range of interest.

The analog signal of each pixel is digitized off chip with a 14 bit 40 Msamples/s ADC (Analog-to-Digital Converter). Each of the 32 ADC channels digitizes the signals of a group of pixels called ‘supercolumn’ (25×200 pixels). The digital signal is measured in ADU (analog-to-digital unit) and it can easily be converted into keV, as explained in section 3.2.

To avoid saturation of the preamplifier due to the higher dark current of GaAs, a shorter exposure time was used for GaAs (6 μs) than for silicon (1 ms). Details on the detector settings used for the experiment are summarized in table 1.

2.2 Experimental setup

The experiments were performed at the TOMCAT beamline [24] of the Swiss Light Source (SLS) using monochromatic photons with an energy ranging between 10 keV and 30 keV, selected using the Si $\langle 111 \rangle$ crystal monochromator.

A 2 μm thick gold pattern on a 200 μm thick silicon wafer fabricated at LMN (PSI) and a tungsten edge were used as imaging samples for comparing the resolution capabilities of the GaAs and silicon sensors. At each energy, flat-field¹ measurements were taken in order to perform the flat-field corrections typically used for imaging detectors [25].

In order to further explore the resolution limits of MÖNCH by means of the position interpolation algorithm, the photons need to be spatially (and temporally) separated to avoid pile-up events, which happens when more than a single photon impinges on the same pixel cluster during the exposure time.

¹A flat-field image is acquired when the detector is uniformly illuminated, thus producing a flat illumination across the detector. The flat-field normalization corrects for the stationary non-uniformities in detector response and beam profile.

In the case of MÖNCH, the single photon regime can be obtained when operated at low photon fluxes and/or short exposure times (e.g., the optimal 1% photon occupancy φ is obtained with a flux of $\sim 3 \times 10^5$ photons/mm²/s with 6 μ s exposure time) [26]. To meet the conditions required for applying the interpolation algorithm (see section 3.3), different combinations of filters were used to attenuate the beam in order to have isolated photons. In this work, data collection was performed with a photon occupancy φ ranging between 2% and 5%.

Due to the required low flux, at least 10 million frames were collected at each energy with and without the sample to have enough statistics to apply the interpolation algorithm. High statistics are necessary because the photons will be redistributed to virtual pixels with pixel dimensions below the native pixel pitch. This implies that by interpolating to 1/10 of the native pixel size, the statistics per virtual pixel are reduced to 1/100.

Since each measurement lasted ~ 160 minutes, and the beam profile and the intensities were not stable during the acquisition, the flat-field corrections did not work properly.

3 Preliminary results

3.1 Characterization of the GaAs sensor

In preparation of the imaging experiments, it was necessary to characterize the GaAs-MÖNCH assembly to understand the performance of the sensor material and readout chip in absence of photons.

The pedestal is the dark signal mainly given by the integrated dark current in the readout chain during a specific exposure time, the sensor conditions (applied bias voltage and sensor temperature) and the gain settings of the preamplifier and CDS. The pedestal also reflects the mismatch between pixels (e.g. reset level, readout offset). The pedestal signal of each pixel can be corrected by acquiring a large number of empty frames $N > 1000$ and subtracting the average value for each pixel. The pedestal value measured in ADU is acquired before and after each experiment to correct for pedestal drifts, which can occur during long data acquisitions.

The standard deviation of the pedestal for each pixel gives an indication of its electronic noise in units of ADU. It is evaluated by fitting a Gaussian function to the distribution of the pedestal peak of each pixel.

An example of the pedestal map acquired with a GaAs:Cr sensor bump-bonded to MÖNCH 03 ASIC with the settings listed in table 1 is shown in figure 1(a). From the pedestal map it is possible to evaluate the quality of the bump-bonding process. Figure 1(a) shows a bump-bonding yield of 99.1 %, excluding the two rows of pixels in the middle of the sensor. This artifact is due to a mistake in the indium mask, creating shorts and some faulty pixels in saturation.

The structures that are visible in the 2D map correspond to dislocation networks and inhomogeneities of the semiconductor crystal [23, 27]. They produce variations of the electric properties of the sensor material, such as local differences in resistivity and charge carrier lifetimes, also reflected in the dark current.

One of the advantages of using small pixels is that it allows the visualization of these structures with a high spatial resolution. Figure 1(b) shows an example of a structure which has dimensions of $\sim 20 \times 25$ pixels (i.e. $500 \times 625 \mu\text{m}^2$ in size) and substructures of the order of a few tens of microns, which would be smeared out using 55–75 μm pixels, as in previous studies [4].

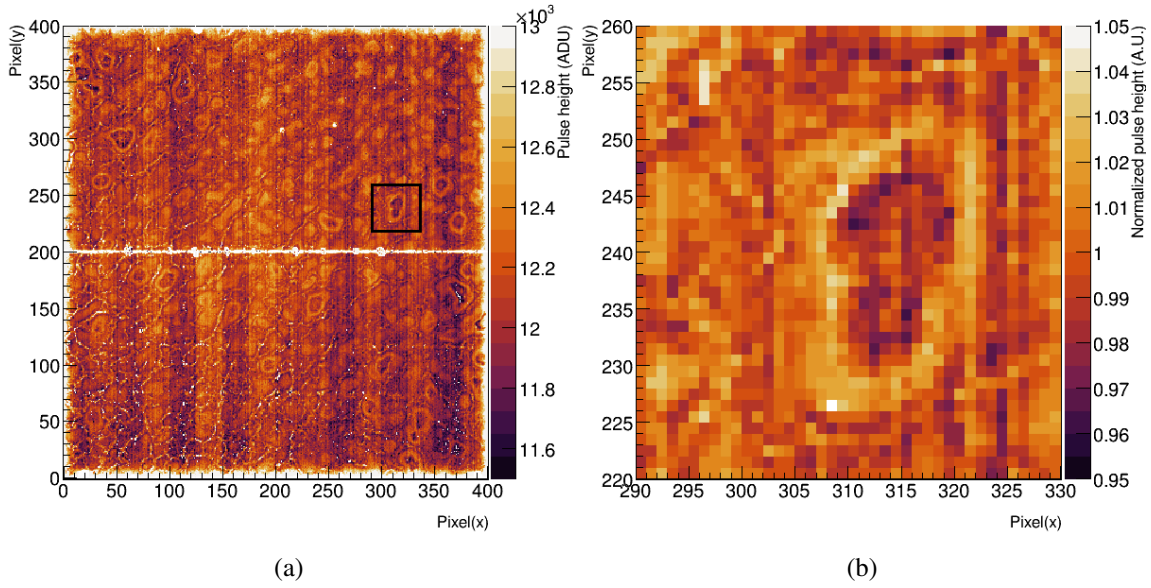


Figure 1. (a) Pedestal map in ADU of a $1 \times 1 \text{ cm}^2$ GaAs-MÖNCH assembly taken with $6 \mu\text{s}$ exposure time, sensor bias voltage of -300 V and $T=+15^\circ\text{C}$. The white region in the middle of the sensor are pixels which were not bump-bonded due to a mistake in the indium mask (see section 3.1). (b) Enlarged image of the region marked in image (a), consisting of an ROI of 40×40 pixels (i.e. $1 \times 1 \text{ mm}^2$), normalized to the maximum value.

3.2 Gain calibration and noise measurement

As a result of the very small pixel size of MÖNCH, there is always a significant amount of charge shared among neighbouring pixels. This effect mainly depends on the sensor material, applied voltage and the energy of the absorbed photon. For instance, in $300 \mu\text{m}$ thick silicon sensors, $\sim 95\%$ of the incoming 16 keV photons share charge with neighboring pixels [26], and a single pixel in most cases only collects a fraction of the charge generated by the incoming photon.

For this reason, in order to retrieve the total energy of the photon, it is necessary to identify all pixels collecting charge generated by the same impinging photon. This is achieved by locating the events where either the signal of a single pixel or the sum of the signals of the neighbors (cluster) is above a certain threshold, defined by a multiple of the electronic noise (usually $5 \times \sigma_e$). When a photon event is identified, pixel clusters of different size are assigned to the pixel collecting the highest signal. A 3×3 pixel cluster consists of the pixels with the highest signal and its neighbors, while clusters of 2×2 pixels are obtained by identifying the 2×2 cluster with the highest signal within the 3×3 cluster. More details about the cluster finder algorithm (CFA) can be found in [22].

The data calibration was performed as follows:

- First, the energy spectra using different cluster sizes were generated for each pixel at each energy, yielding the cluster spectra as shown in figure 2. This figure shows an example of the energy spectra of 16 keV photons for an arbitrarily chosen pixel of the GaAs-MÖNCH assembly for different cluster sizes 2×2 (blue curve) and 3×3 (green curve) together with the single channel spectrum (black curve) and central pixel (red curve). The x -axis is expressed in ADU units.

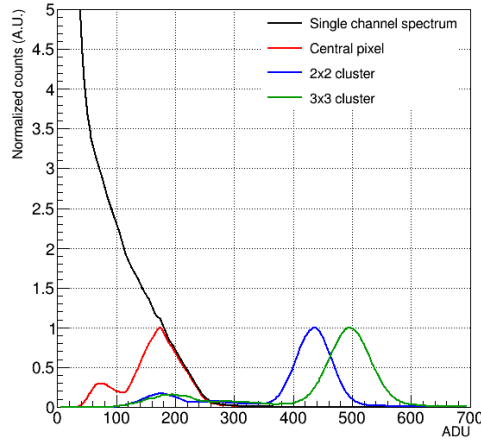


Figure 2. Comparison of single channel spectrum (black curve), central pixel (red curve) and, the 2×2 and 3×3 cluster spectra for a single pixel measured at 16 keV photons in ADU units (see section 3.2).

The single channel spectrum (black curve) represents the value of the pixel whenever it belongs to a cluster detected by the algorithm and no peak is visible because a single pixel only collects a fraction of the charge generated by a photon. The central pixel curve (red curve) takes into account only the pixel with the highest signal of the 3×3 cluster and reflects the fact that the charge is never collected by a single pixel, because of the dimension of the charge cloud with respect to the pixel pitch. The photon peak at ~ 180 ADU is due to the partial collection of the charge generated by 16 keV photons and the lower peak at ~ 80 ADU is probably arising from the escape peaks of the fluorescence of Ga and As. The central pixel collects $\sim 35\%$ of the total charge in comparison to the 3×3 cluster spectrum. The photon peak of the 3×3 clusters at ~ 495 ADU (green curve) is related to the photon energy of 16 keV and the smaller peak around ~ 200 ADU corresponds to the escape peaks of Ga and As, while in the case of the 2×2 clusters the photon peak is at ~ 435 ADU (and at about ~ 180 ADU for the escape peak). A slightly increase of the peak width of the 3×3 cluster spectrum (7.4% with respect to 6.9%) is due to the higher number of pixels in the pixel cluster contributing to the overall noise of the spectrum. Also, as can be seen in the figure, the photon peak position is reduced compared to the spectra of the 3×3 clusters, since the 2×2 cluster-size does not contain all the charge deposited by the absorbed photons. Therefore, the 3×3 cluster was used for the calculation of the gain map and for the interpolation algorithm, in order to achieve a more accurate measurement of the spatial and energy resolution.

- Secondly, a single pixel calibration was performed by assigning the total signal of a cluster to the pixel with the highest signal and by fitting the 3×3 cluster spectrum obtained with a Gaussian function. The gain i.e., the energy conversion factor in ADU/keV was obtained for each pixel by normalizing the peak position to the photon energy.

Figure 3(a) shows an example of the gain map, while figure 3(b) shows the corresponding gain distribution over the full sensitive area of the detector. The dislocation networks are visible in the gain map.

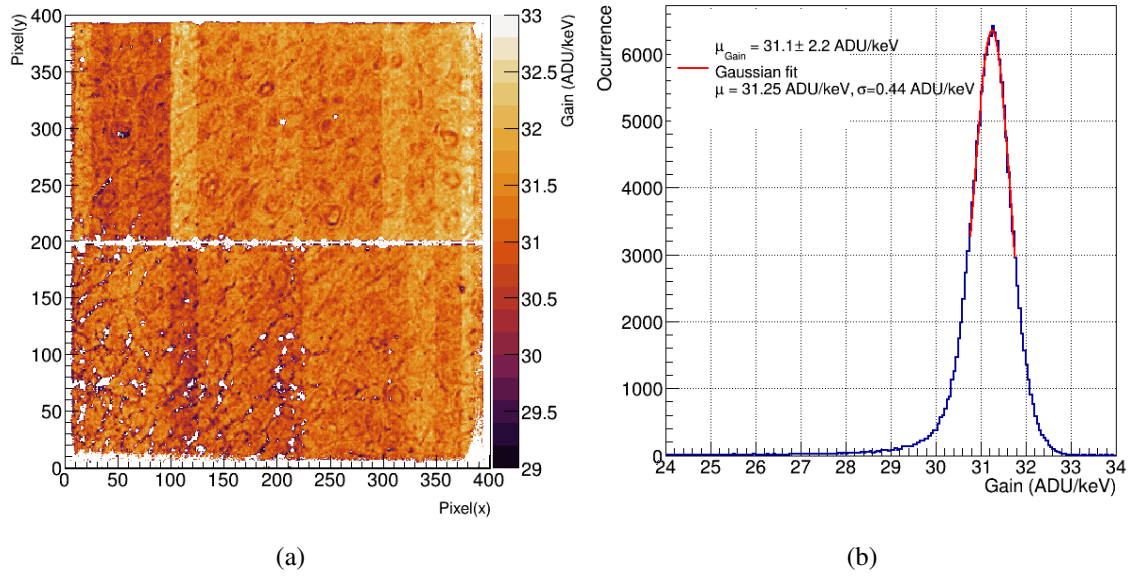


Figure 3. (a) Gain map of the sensor measured with 12 keV photons. The white areas in the bottom part are faulty pixels in which the 3×3 cluster spectrum could not be calculated. (b) The corresponding gain distribution over the full sensitive area of the detector (blue line) indicates the average gain μ_{gain} . The red line shows the Gaussian fit of the peak and the corresponding mean gain value as μ .

A mean gain value of $\mu_{\text{gain}} = (31.1 \pm 2.2)$ ADU/keV was measured in G1HG settings. The gain map is approximately uniform over the active area of the detector with a variation of less than 7% (r.m.s). A major contribution to the gain variation is due to the gain variations of the output buffer, visible in the vertical 25 pixel wide columns (supercolumns) of slightly different gain.

After applying the gain conversion factor of each pixel to the noise of each pixel in units of ADU and, using the electron-hole pair creation energy of $W_{\text{GaAs}} = 4.2$ eV in GaAs [23], the noise is converted to ENC (Equivalent Noise Charge) i.e., the signal at the input of the preamplifier which would result in the measured noise value [28]. We found an average electronic noise of $\sigma_e = 80.4 \pm 9.5$ e⁻ ENC, equivalent to 338 ± 40 eV.

Figure 4 shows the 3×3 cluster energy spectra for a region of interest (ROI) of pixels² calibrated using the gain value of each pixel at different photon energies in the range between 10 keV and 30 keV. All energy spectra contain the escape peaks due to fluorescence photons from Ga and As. For instance, the spectrum at 30 keV has two additional peaks at 10 keV, coming from fluorescence photons of Ga or As which were not absorbed within the 3×3 pixel cluster³, and an escape peak at 20 keV, corresponding to the difference between the primary photon energy of 30 keV and the energy of the fluorescence photons which escape the pixel cluster. The high energy tail which is visible in

²An ROI was selected to ensure comparability of the results at the different photon energies because at the TOMCAT beamline, the vertical size of the beam becomes smaller for higher energies, and we could not cover the same field of view as at low energies.

³The absorption K-edges for Ga and As are 10.37 keV and 11.87 keV, respectively. As a result, fluorescence photons are emitted at $E_{\text{Ga K}\alpha 1} = 9.25$ keV and $E_{\text{As K}\alpha 1} = 10.54$ keV. The mean free paths of these fluorescence photons are 40.6 μm and 15.6 μm , respectively [29].

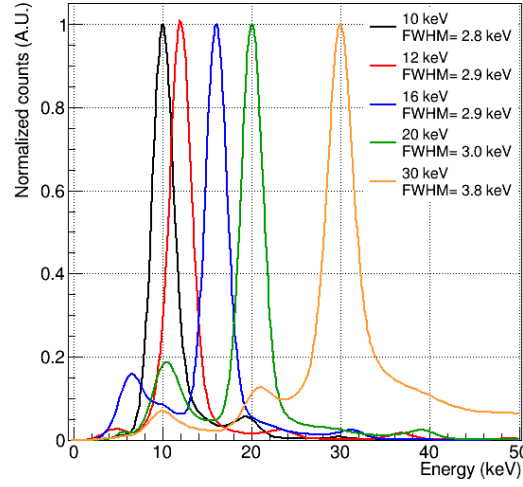


Figure 4. Comparison of the 3×3 cluster energy spectra after calibrating each pixel with its conversion gain factor for an ROI of 180×147 pixels at different energies between 10 keV and 30 keV. Spectra have been normalized to the photon peak for comparison.

Table 2. Measured energy resolution compared to the ideal one calculated from the electronic noise and the fluctuation of the generated charge carriers as a function of the photon energy and of the photon occupancy.

E (keV)	FWHM _{meas} (keV)	FWHM _{meas} /E (%)	FWHM _{Fano} (keV)	FWHM _{noise} (keV)	FWHM _{meas} /FWHM _{theo} (%)	φ (%)
10	2.80	28.0	0.071	2.38	117.6	3
12	2.92	24.3	0.077	2.38	122.7	2
16	2.87	17.9	0.090	2.38	120.6	2
20	3.02	15.1	0.100	2.38	126.7	3
30	3.82	12.7	0.123	2.38	160.5	5

the spectra, particularly at 30 keV, is due to pile-up photons arising from the photon occupancy used during the measurement which was slightly too high.

The measured full width half maximum (FWHM_{meas}), calculated from fitting the photon peak with a Gaussian, ranges from 2.8 to 3.8 keV at 10 keV and 30 keV, respectively (see table 2). The energy resolution is mainly determined by the electronic noise, $\text{FWHM}_{\text{noise}} = 2.35 \times \sqrt{9} \times \sigma_e \times W_{\text{GaAs}} = 2.38$ keV, while the fluctuations of the primary charge-carrier creation are negligible $\text{FWHM}_{\text{Fano}} = W_{\text{GaAs}} \times \sqrt{F \times E / W_{\text{GaAs}}}$ (about 120 eV at 30 keV considering a Fano Factor $F=0.12$ [30]).

However, we can see that FWHM_{meas} is larger than $\text{FWHM}_{\text{theo}} = \sqrt{\text{FWHM}_{\text{noise}}^2 + \text{FWHM}_{\text{Fano}}^2}$ ($\sim 18\%$ at 10 keV up to $\sim 60\%$ at 30 keV) mainly due to fluorescence and high photon occupancy. A high photon occupancy gives rise to a high energy tail of the photon peak which deteriorates the energy resolution, due to charge coming from photons absorbed in neighboring pixels, as visible in figure 4. The energy resolution is also affected by the energy dependence of the fluorescence yield, which is absent at 10 keV (below the K-edges of Ga and As at 10.4 keV and 11.9 keV, respectively) and is maximum just above the K-edges of Ga and As i.e., at 12 keV in the case of the energies used

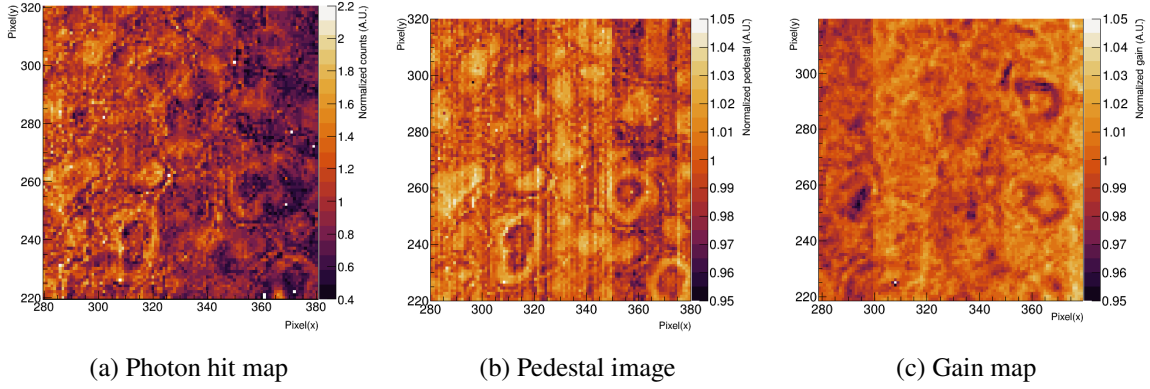


Figure 5. Zoom of the (a) flat field image at 16 keV, (b) pedestal map and (c) gain map for the same ROI of 100×100 pixels ($2.5 \times 2.5 \text{ mm}^2$). For comparison purposes, the distributions have been normalized to the mean value.

in this study [31], since the CFA can not distinguish between primary photons and the fluorescence photons. In particular, Ga fluorescence photons can escape out of the 3×3 pixel cluster, due to their $40 \mu\text{m}$ absorption length, which is larger than the pixel pitch of the detector. Increasing the cluster size by adding more pixels would mitigate this effect, but still deteriorating the energy resolution due to the summation of the electronic noise of more channels and increasing of the pile up tail.

The detector response to a uniform radiation field (flat field) is shown in figure 5(a), which corresponds to the 2D hit map acquired at 16 keV energy photons. The structures visible in the flat-field image correspond to similar artefacts in the pedestal and in the gain map (see figure 5(b), 5(c)), indicating that there is a correlation between these quantities. These structures are probably due to the dislocation network and defects of the crystal which affect the electric field and therefore the charge collection [10, 13]. Since the structures of the sensor are stable in time it is possible to subtract the pedestal signal, gain correct, and flat-field normalize the images. However, this motivates a study of their effects on the imaging performance of the detector.

3.3 Position interpolation algorithm

The position interpolation algorithm is based on the η algorithm previously used in strip detectors [32]. The η variable corresponds to the linearly interpolated position and its non-uniform distribution is a consequence of the position-dependence of the charge sharing. In previous works we have applied an optimized version of the interpolation algorithm described in [14, 22], which compares the signals of adjacent pixels to improve the position resolution for imaging applications based on the cluster spectrum. The performance of this algorithm was evaluated for the MÖNCH detector with a silicon sensor where a spatial resolution of the order of a few μm was achieved [15].

In this work we have adapted the interpolation algorithm employing a different η distribution (equation (3.1)) by using 3×3 clusters for the interpolation. The first step of the adapted interpolation algorithm takes as input a flat-field illuminated image. From this image, the 3×3 clusters are extracted (see figure 2 in section 3.2 for more information) and a global η -distribution map $H(\eta_x, \eta_y)$ is calculated using all hits of all pixels together. η_x and η_y are generated to calculate the interaction

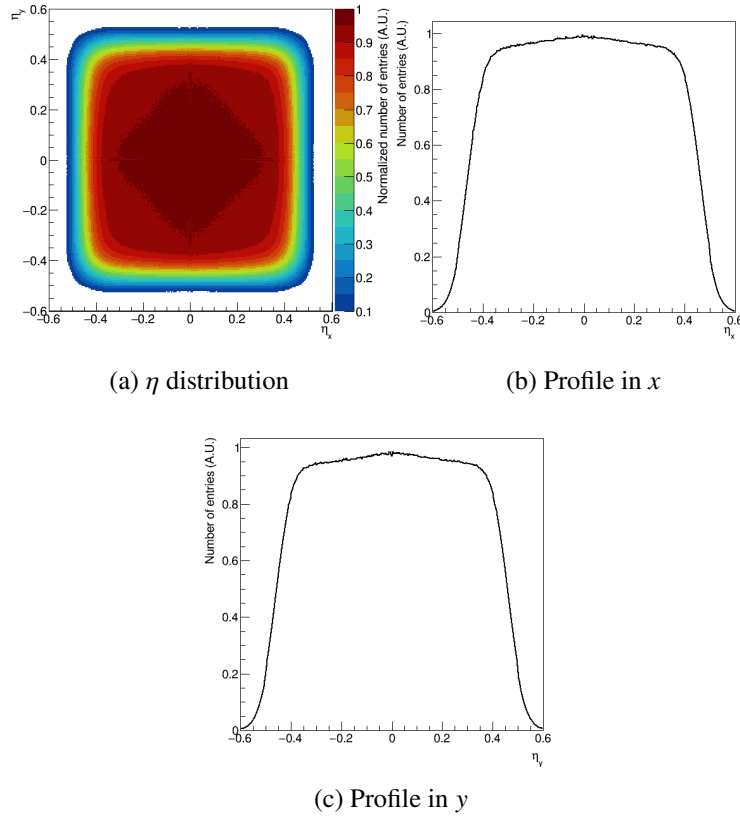


Figure 6. (a) 2-dimensional η -distribution calculated for 16 keV energy photons. The distribution is relatively flat, meaning that for all positions there is a significant amount of charge sharing. (b) Profile along the x axis at $\eta_y = 0$. (c) Profile along the y axis at $\eta_x = 0$.

point of the impinging photons with respect to the geometrical center of the cluster using:

$$\eta_x = \frac{-L+R}{L+C+R}, \quad \eta_y = \frac{-B+T}{T+C+B}, \quad (3.1)$$

where L , R , T , B are the signals of the left, right, top, and bottom of the indicated pixel position with respect to the channel with the highest signal (C , center) in the 3×3 pixel matrix. The shape of the η -distribution varies with the photon energy, applied bias voltage and sensor thickness because all these parameters affect the charge sharing among adjacent pixels. Therefore, the η distribution was calculated for each photon energy.

An example of the 2-dimensional η -distribution obtained using equation (3.1) is plotted in figure 6 and it illustrates the high amount of charge sharing. By definition, the distribution should range between -0.5 and $+0.5$, where -0.5 corresponds to the left (or bottom), $+0.5$ to the right (or top) boundary and 0 to the center of the pixel. However, η can reach values lower than -0.5 or higher the $+0.5$ due to noise.

3.4 High resolution imaging with GaAs

A comparison of the non-interpolated images acquired at 16 keV is shown in figure 7 for Si (a) and GaAs (c), respectively.

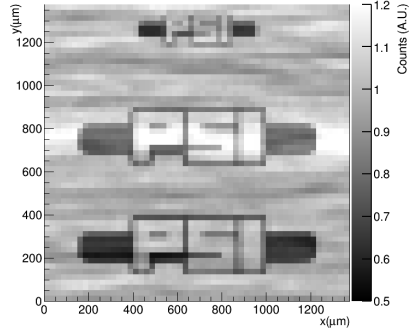
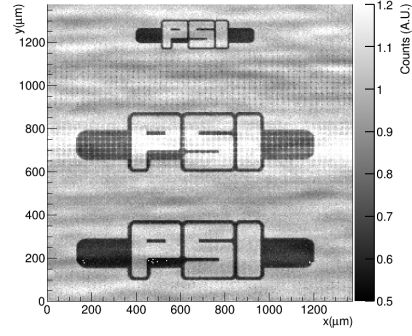
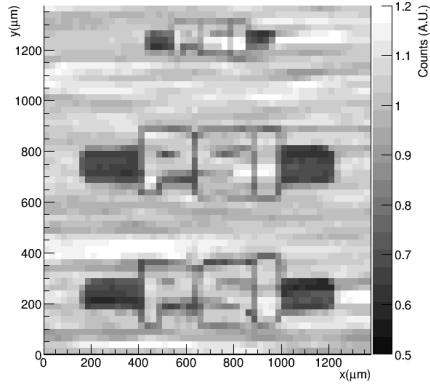
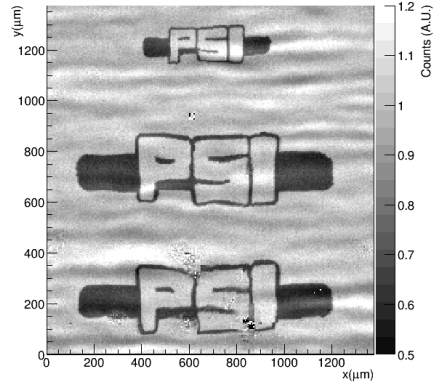
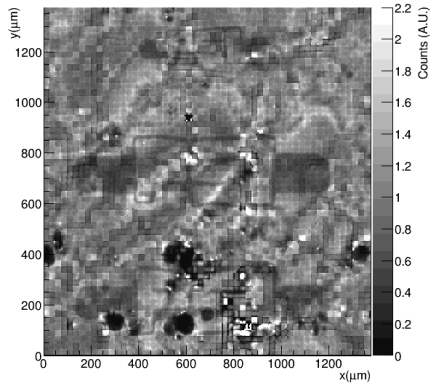
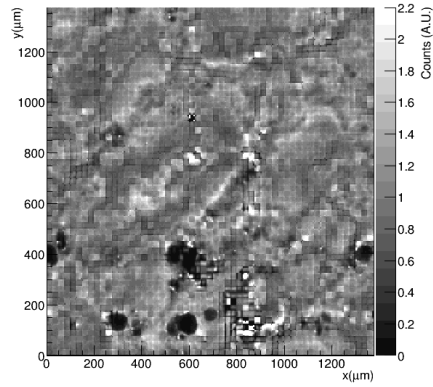
(a) Si, native resolution 25 μm (b) Si, interpolated to 5 μm (c) GaAs, native resolution 25 μm (d) GaAs, interpolated to 5 μm (e) GaAs sample, interpolated to 5 μm (f) GaAs flat-field, interpolated to 5 μm

Figure 7. Non-interpolated image of the PSI logo measured with the Si (a) and GaAs (c) sensors at 16 keV photons before applying the interpolation algorithm (25 μm bins). (b) and (d) show the interpolated images binned to 5 μm virtual bins for Si (b) and GaAs (d) sensors. (e) and (f) are the uncorrected sample and flat-field images (both interpolated and binned to 5 μm virtual pixels), respectively, for GaAs.

The data processing of the non-interpolated images was performed as follows: the analog signal of each pixel was gain corrected using the gain map (see section 3.2), and the gain calibrated 3×3 pixel cluster spectrum was calculated. Only the photons whose energies deviated less than 10% from the incident beam energy were used, in order to remove events not related to single primary beam photons e.g., reject pile-up, fluorescence and third harmonics. Then, the photon hit map was obtained for the sample and the flat-field measurements, respectively. The resulting 2D hit map of the sample was flat-field corrected as explained in [25].

The same procedure was performed for the interpolated images. Additionally, the η -distribution using the 3×3 pixel cluster spectra of the flat field was calculated at each energy (see figure 6 as an example). To apply the interpolation algorithm down to $5 \mu\text{m}$, each pixel position was binned into virtual pixels by subdividing the physical pixel into 5×5 bins. The interpolated images down to $5 \mu\text{m}$ virtual pixels are shown in figure 7 for Si (b) and GaAs (d). In the interpolated image acquired with silicon, we can observe artefacts appearing like dots with the same periodicity as the physical pixel size. These are systematic effects due to the highly non-linear η -distributions. These artefacts can partially be corrected with more advanced interpolation algorithms which have not been applied in this work [15] and disappear in the images acquired using gallium arsenide, where the photons are absorbed closer to the entrance side of the sensor and thus generate more charge sharing.

Two types of distortions can be distinguished in the processed images:

- The first type comes from the instability of the beam intensity causing ripples and strong variations in areas that would be expected to display a uniform background. These ripples can be seen in all images with silicon and GaAs sensors (non-interpolated and interpolated) of figure 7. This instability of the beam over time caused several issues regarding the reliability of the flat-field correction, which even becomes barely usable at 30 keV.
- The second type of distortions is due to the electric properties of the GaAs sensor material (more details in section 3.1) and don't appear in the images acquired with the silicon sensor. The distortions (waves) are already visible in the letters of the PSI logo for the non-interpolated image (figure 7(c)) but they get enhanced after applying the interpolation algorithm (figure 7(d)).

Figure 7(e) and figure 7(f) show the interpolated image of the sample and the flat field, without normalization. The contrast due to the defects of the sensors material is much higher than the one from the sample, which is barely visible in absence of the flat-field corrections. The images were binned to $5 \mu\text{m}$ for the same ROI of 50×50 pixels and illustrate that the crystalline imperfections of GaAs affect the imaging capability. The crystal defects potentially cause distortions of the electric field near the 'S' of the PSI logo (e.g. in the central logo). Moreover, these second type of distortions are not visible in the images acquired with Si-MÖNCH. Therefore, we assume that they are caused by defects and non-uniformities in the GaAs sensor. The distortions due to the sensor material were already observed with a JUNGFRÄU GaAs detector [11], where measurements with collimated pencil beams indicated different effective pixel sizes in comparison to the physical pixel pitch of the detector.

By using a global η function, averaged on all pixels, we assume that the effective pixel size is uniform over the whole sensor. However, previous measurements have revealed variations of the effective pixel size in GaAs:Cr sensors [11, 13, 18] and, consequently, using a global η distribution

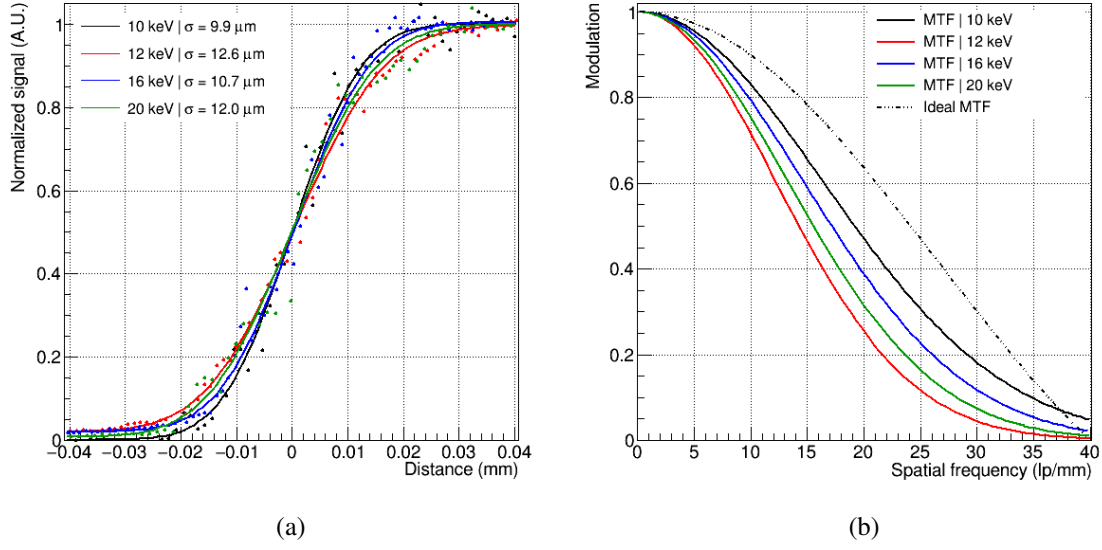


Figure 8. (a) ESF distribution processed for GaAs for 10, 12, 16 and 20 keV. Processed ESF (dots) and fitted curve with the equation (3.2) (line). The σ values (indicating the spatial resolution) are obtained from the fit. (b) MTFs of GaAs for different photon energies (solid lines) together with the ideal MTF (calculated with equation (3.3), dashed line) for comparison.

might also cause problems with the position interpolation. Therefore, further improvements of the interpolation algorithm using single- η distributions calculated for each pixel are under development to evaluate whether the deformations in the interpolated image can be removed.

3.5 Measurement of the modulation transfer function (MTF)

The modulation transfer function (MTF) was calculated using the slanted-edge method [33] to quantify the spatial resolution of GaAs and Si sensors. To determine the MTF the following steps were performed:

- From the processed 2D hit image, an ROI containing the slanted-edge is selected.
- The angle of the slanted edge is determined by the linear regression of the edge location and the row. This is performed by projecting the pixels in the ROI along the direction of the estimated edge onto the horizontal x -axis, and by fitting an erf function, the edge position is determined for each pixel row with pixel accuracy. By knowing the tilt angle, each pixel row is shifted by the known angle, so that the slanted-edge is aligned along the y -direction.
- Then an over-sampled Edge Spread Function (ESF) is built by projecting the aligned 2D photon map of the slanted edge of each row along the edge into a one dimensional representation.

The derivative of the ESF was then calculated to obtain the Line Spread Function (LSF). Ultimately, the absolute value of the Fourier transform of the LSF is calculated to obtain the MTF, plotted in figure 8(b).

Figure 8(a) illustrates the measured ESF distributions with GaAs for photon energies of 10, 12, 16 and 20 keV. The ESF was fitted with the integral of a Gaussian:

$$f(x) = \frac{A}{2} \left(1 + \operatorname{Erf} \left(\frac{x - \mu}{\sqrt{2}\sigma} \right) \right) + B \quad (3.2)$$

where σ is the width of the error function, μ is the mean position of the edge, A is a normalization factor related to the amplitude of the curve, and B is a constant. From the σ value of the fitting function, an estimation of the spatial resolution can be obtained at each energy.

As can be seen from figure 8(a), the spatial resolution obtained with GaAs at 10 keV is $\sim 10 \mu\text{m}$ in comparison to $7.22 \mu\text{m}$, which is the resolution of an ideal detector⁴ with a pixel pitch of $25 \mu\text{m}$ (a difference of 27%). The spatial resolution is better at 10 keV than at higher energies. A possible explanation is that there are no fluorescence photons from Ga and As at 10 keV, as the K-edge is at 10.37 keV and 11.87 keV, respectively.

In figure 8(b) the corresponding MTF distributions for photon energies of 10, 12, 16 and 20 keV photon energies obtained from fitting the ESF curves are plotted up to the Nyquist frequency = 40 lp/mm⁵, together with the ideal MTF pixel response. The ideal MTF is calculated using [1, 34]:

$$\text{MTF}_{\text{ideal}} = \frac{\sin(\pi \nu d)}{\pi \nu d} \quad (3.3)$$

where ν is the spatial frequency and d is the pixel pitch.

Figure 9(a) illustrates the ESF distributions at 16 keV photon energy for GaAs without interpolation in comparison to different interpolated virtual bins down to $2.5 \mu\text{m}$, together with the response of silicon measured at the same bin size. An improvement of about a factor 2 in the resolution is achieved when comparing the non-interpolated with the interpolated images down to $2.5 \mu\text{m}$. A resolution of approximately $5 \mu\text{m}$ is achieved when binning to $2.5 \mu\text{m}$. Figure 9(b) shows the corresponding MTF calculated from the ESF fit at each bin size for GaAs (line) together with the calculated Si (dashed line) for comparison. The resolution obtained with a $650 \mu\text{m}$ thick silicon sensor was $\sim 8.5 \mu\text{m}$ with 16 keV photons and $\sim 3.5 \mu\text{m}$ after interpolation to $2.5 \mu\text{m}$ virtual bins. The resolution obtained with a $500 \mu\text{m}$ GaAs:Cr sensor was $\sim 10.7 \mu\text{m}$ with 16 keV photons (fig 9(a)) and $\sim 5.1 \mu\text{m}$ after interpolation to $2.5 \mu\text{m}$ virtual bins. At this energy, the spatial resolution obtained after interpolation with GaAs differs by about 30 % when compared to a $650 \mu\text{m}$ thick silicon sensor.

4 Conclusion and outlook

The MÖNCH 03 detector is a unique tool to study different sensor materials due to the very small pixel size and the analogue information measured for each pixel.

We have reported on the first imaging experiments performed with a GaAs-MÖNCH assembly to measure the spatial resolution of $25 \mu\text{m}$ GaAs pixels at photon energies between 10 and 30 keV, carried out at the TOMCAT beamline. Moreover, an interpolation method was employed, which, in a first approximation was successful, as it improved the achievable spatial resolution of GaAs-MÖNCH

⁴In the ideal case, σ is calculated from the standard deviation of a uniform distribution to be $\sigma = d/\sqrt{12}$, where d is the pixel pitch [34].

⁵The Nyquist frequency is defined as $f_N = 1/d$, where d is the pixel pitch.

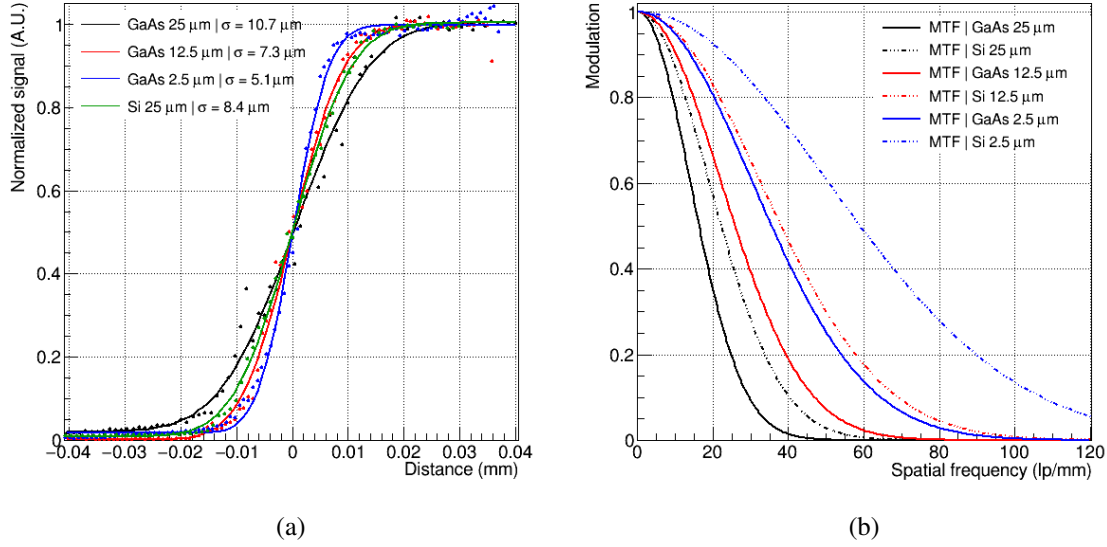


Figure 9. (a) ESF distribution at 16 keV for GaAs without interpolation and different virtual interpolating bins down to 2.5 μm . Measured ESF (dots) and fit with equation (3.2) (line) (b) The corresponding MTF obtained from a fast Fourier transform (FFT) of the ESF fit for the corresponding bin size for GaAs (line) together with the MTF obtained with the silicon (dashed line) at the same energy and bin size.

at 16 keV by about a factor 2 when binning the image to $2.5 \times 2.5 \mu\text{m}^2$ virtual pixels. The distortions observed in the processed images are due to non-uniformities in the crystal structure of GaAs:Cr and the spatial resolution obtained before and after the interpolation algorithm differed by about 20–30% when compared to the Si-MÖNCH assembly. Further analysis using individual η -distributions computed for each pixel will be carried out to understand whether an improved version of the interpolation algorithm can correct some of the distortions due to the electric properties of GaAs.

However, one of the main limitations of this study was the instability of the beam that we faced during the measurements at the beamline. We expect that the results are partially affected by the poor quality of the flat-field corrections, which are needed to correct for the strong patterns of the GaAs sensor.

Overall, these preliminary results encourage the usage of the interpolation algorithm to obtain sub-pixel resolution with MÖNCH with GaAs sensors for imaging applications at high photon energies. Further measurements with an X-ray micro-focus tube are under way to exploit the capabilities of this detector for high resolution energy-resolved imaging.

Acknowledgments

We acknowledge the Paul Scherrer Institut, Villigen, Switzerland for provision of synchrotron radiation beamtime at the TOMCAT beamline X02DA of the Swiss Light Source (SLS) and would like to thank C.M. Schlepütz for assistance. This project has received funding from the European Union’s Horizon 2020 research and innovation program under the Marie Skłodowska-Curie grant agreement no. 884104 (PSI-FELLOW-III-3i).

References

- [1] J. Scholz, L. Birnbacher, C. Petrich, M. Riedel, L. Heck, S. Gkoumas et al., *Biomedical x-ray imaging with a GaAs photon-counting detector: A comparative study*, *APL Photon.* **5** (2020) 106108.
- [2] M. Berger, J. Hubbell, S. Seltzer, J. Chang, J. Coursey, R. Sukumar et al., *XCOM: Photon cross section database (version 1.5)*, National Institute of Standards and Technology (2010), DOI: [10.18434/T48G6X](https://doi.org/10.18434/T48G6X).
- [3] P. Smolyanskiy, B. Bergmann, G. Chelkov, S. Kotov, U. Kruchonak, D. Kozhevnikov et al., *Properties of GaAs:Cr-based Timepix detectors*, *2018 JINST* **13** T02005 [[arXiv:1712.03369](https://arxiv.org/abs/1712.03369)].
- [4] E. Hamann, A. Cecilia, A. Zwerger, A. Fauler, O. Tolbanov, A. Tyazhev et al., *Characterization of photon counting pixel detectors based on semi-insulating GaAs sensor material*, *J. Phys. Conf. Ser.* **425** (2013) 062015.
- [5] P. Zambon, *Simulation of polarization dynamics in semi-insulating, Cr-compensated GaAs pixelated sensors under high x-ray fluxes*, *AIP Adv.* **11** (2021) 075006.
- [6] B.L. Henke, E.M. Gullikson and J.C. Davis, *X-Ray Interactions: Photoabsorption, Scattering, Transmission, and Reflection at $E = 50\text{--}30000$ eV, $Z = 1\text{--}92$* , *Atom. Data Nucl. Data Tabl.* **54** (1993) 181 [<https://henke.lbl.gov/>].
- [7] A. Thompson, *X-ray data booklet*, Lawrence Berkeley National Laboratory, University of California, 2009, <https://xdb.lbl.gov>.
- [8] A. Tyazhev, D. Budnitsky, O. Koretskay, V. Novikov, L. Okaevich, A. Potapov et al., *GaAs radiation imaging detectors with an active layer thickness up to 1mm*, *Nucl. Instrum. Meth. A* **509** (2003) 34.
- [9] M. Veale, S. Bell, D. Duarte, M. French, M. Hart, A. Schneider et al., *Investigating the suitability of GaAs:Cr material for high flux x-ray imaging*, *2014 JINST* **9** C12047.
- [10] D. Greiffenberg, M. Andrä, R. Barten, A. Bergamaschi, P. Busca, M. Brückner et al., *Characterization of GaAs:cr sensors using the charge-integrating JUNGFR AU readout chip*, *2019 JINST* **14** P05020.
- [11] D. Greiffenberg, M. Andrä, R. Barten, A. Bergamaschi, M. Brückner, P. Busca et al., *Characterization of chromium compensated GaAs sensors with the charge-integrating JUNGFR AU readout chip by means of a highly collimated pencil beam*, *Sensors* **21** (2021) 1550.
- [12] R. Wheeler, L. Jowitt, S. Richards, M. Veale, M. Wilson, O. Fox et al., *X-ray microbeam characterisation of crystalline defects in small pixel gaas:cr detectors*, *Nucl. Instrum. Meth. A* **999** (2021) 165207.
- [13] J. Becker, M.W. Tate, K.S. Shanks, H.T. Philipp, J.T. Weiss, P. Purohit et al., *Characterization of Chromium Compensated GaAs as an x-ray Sensor Material for Charge-Integrating Pixel Array Detectors*, *2018 JINST* **13** P01007 [[arXiv:1707.02189](https://arxiv.org/abs/1707.02189)].
- [14] S. Cartier, A. Bergamaschi, R. Dinapoli, D. Greiffenberg, I. Johnson, J.H. Jungmann et al., *Micron resolution of MÖNCH and GOTTHARD, small pitch charge integrating detectors with single photon sensitivity*, *2014 JINST* **9** C05027.
- [15] S. Cartier, M. Kagias, A. Bergamaschi, Z. Wang, R. Dinapoli, A. Mozzanica et al., *Micrometer-resolution imaging using MÖNCH: towards G_2 -less grating interferometry*, *J. Synchrotron Radiat.* **23** (2016) 1462.
- [16] A. Bergamaschi, M. Andrä, R. Barten, C. Borca, M. Brückner, S. Chiriotti et al., *The MÖNCH detector for soft x-ray, high-resolution, and energy resolved applications*, *Synchrotron Radiat. News* **31** (2018) 11.

- [17] E. Hamann, T. Koenig, M. Zuber, A. Cecilia, A. Tyazhev, O. Tolbanov et al., *Performance of a medipix3rx spectroscopic pixel detector with a high resistivity gallium arsenide sensor*, *IEEE Trans. Med. Imaging* **34** (2015) 707.
- [18] K.A. Paton, M.C. Veale, X. Mu, C.S. Allen, D. Maneuski, C. Kübel et al., *Quantifying the performance of a hybrid pixel detector with GaAs:Cr sensor for transmission electron microscopy*, *Ultramicroscopy* **227** (2021) 113298.
- [19] E.S. Dreier, A. Bergamaschi, G.K. Kallon, R. Brönnimann, U.L. Olsen, A. Olivo et al., *Tracking based, high-resolution single-shot multimodal x-ray imaging in the laboratory enabled by the sub-pixel resolution capabilities of the MÖNCH detector*, *Appl. Phys. Lett.* **117** (2020) 264101.
- [20] R. Dinapoli, A. Bergamaschi, S. Cartier, D. Greiffenberg, I. Johnson, J.H. Jungmann et al., *MÖNCH, a small pitch, integrating hybrid pixel detector for x-ray applications*, *2014 JINST* **9** C05015.
- [21] W. Buttler, B. Hosticka and G. Lutz, *Noise filtering for readout electronics*, *Nucl. Instrum. Meth. A* **288** (1990) 187.
- [22] M. Ramilli et al., *Measurements with MÖNCH, a 25 μm pixel pitch hybrid pixel detector*, *2017 JINST* **12** C01071.
- [23] E. Hamann, *Characterization of high resistivity GaAs as sensor material for photon counting semiconductor pixel detectors*. PhD thesis, Albert-Ludwigs-Universität Freiburg im Breisgau, 2013.
- [24] M. Stampanoni, A. Groso, A. Isenegger, G. Mikuljan, Q. Chen, D. Meister et al., *TOMCAT: A beamline for tomographic microscopy and coherent radiology experiments*, *AIP Conf. Proc.* **879** (2007) 848–851.
- [25] J.A. Seibert, J.M. Boone and K.K. Lindfors, *Flat-field correction technique for digital detectors*, *Proc. SPIE* **3336** (1998) 348.
- [26] A. Bergamaschi, S. Cartier, R. Dinapoli, D. Greiffenberg, J.H. Jungmann-Smith, D. Mezza et al., *Looking at single photons using hybrid detectors*, *2015 JINST* **10** C01033.
- [27] P. Rudolph, *Dislocation cell structures in melt-grown semiconductor compound crystals*, *Cryst. Res. Technol.* **40** (2005) 7.
- [28] V. Radeka, *Low Noise Techniques in Detectors*, *Ann. Rev. Nucl. Part. Sci.* **38** (1988) 217.
- [29] L. Tlustos, *Performance and limitations of high granularity single photon processing X-ray imaging detectors*, Ph.D. thesis, TU Wien (2005).
- [30] G. Bertuccio, A. Pullia, J. Lauter, A. Forster and H. Luth, *Pixel x-ray detectors in epitaxial gallium arsenide with high-energy resolution capabilities (fano factor experimental determination)*, *IEEE Trans. Nucl. Sci.* **44** (1997) 1.
- [31] M.L. Garg, D. Mehta, S. Kumar, P.C. Mangal and P.N. Trehan, *Energy dependence of photon-induced $k\alpha$ and $k\beta$ x-ray fluorescence cross-sections for some elements with $20 \leq z \leq 56$* , *X-Ray Spectrom.* **14** (1985) 165.
- [32] A. Schubert, A. Bergamaschi, C. David, R. Dinapoli, S. Elbracht-Leong, S. Gorelick et al., *Micrometre resolution of a charge integrating microstrip detector with single photon sensitivity*, *J. Synchrotron Radiat.* **19** (2012) 359.
- [33] E. Samei, M.J. Flynn and D.A. Reimann, *A method for measuring the presampled MTF of digital radiographic systems using an edge test device*, *Med. Phys.* **25** 102–113.
- [34] S.N. Ahmed, *7 - Position-sensitive detection and imaging*, in *Physics and Engineering of Radiation Detection (Second Edition)*, S.N. Ahmed, ed., second edition, Elsevier (2015), pp. 435–475.